Variational Stokes: A Unified Pressure-Viscosity Solver for Accurate Viscous Liquids

EGOR LARIONOV*, University of Waterloo
CHRISTOPHER BATTY*, University of Waterloo
ROBERT BRIDSON, Autodesk Canada

Fig. 1. By carefully treating coupling between viscosity and pressure forces, our unified Stokes-based fluid solver can reproduce the classic liquid rope coiling instability of viscous liquids like honey, while prior grid-based methods cannot.

We propose a novel unsteady Stokes solver for coupled viscous and pressure forces in grid-based liquid animation which yields greater accuracy and visual realism than previously achieved. Modern fluid simulators treat viscosity and pressure in separate solver stages, which reduces accuracy and yields incorrect free surface behavior. Our proposed implicit variational formulation of the Stokes problem leads to a symmetric positive definite linear system that gives properly coupled forces, provides unconditional stability, and treats difficult boundary conditions naturally through simple volume weights. Surface tension and moving solid boundaries are also easily incorporated. Qualitatively, we show that our method recovers the characteristic rope coiling instability of viscous liquids and preserves fine surface details, while previous grid-based schemes do not. Quantitatively, we demonstrate that our method is convergent through grid refinement studies on analytical problems in two dimensions. We conclude by offering practical guidelines for choosing an appropriate viscous solver, based on the scenario to be animated and the computational costs of different methods.

CCS Concepts: • **Computing methodologies** → **Physical simulation**; **Continuous simulation**;

Additional Key Words and Phrases: liquids, free surfaces, Stokes, viscosity

ACM Reference format:
Egor Larionov*, Christopher Batty*, and Robert Bridson. 2017. Variational Stokes: A Unified Pressure-Viscosity Solver for Accurate Viscous Liquids. *ACM Trans. Graph.* 36, 4, Article 101 (July 2017), 11 pages.
DOI: http://dx.doi.org/10.1145/3072959.3073628

*Joint first authors.

0730-0301/2017/7-ART101 $15.00
DOI: http://dx.doi.org/10.1145/3072959.3073628

1 INTRODUCTION

Tar, honey, and molasses are familiar examples of viscous liquids which exhibit an array of intriguing effects, including damped motion, buckling, meandering, and even rope-like coiling. Given the ubiquity of such liquids, there is a strong demand for simulation tools that can reproduce their behavior for animation and visual effects scenarios, such as melting terminators [Rasmussen et al. 2004], flowing tar monsters [Wiebe and Houston 2004], and spilling honey [Ruilova 2007]. Viscous liquids are also relevant to other industries, such as container filling for food processing and cosmetics [Tomé and McKee 1999]. While various complex non-Newtonian liquids [Stomakhin et al. 2014; Yue et al. 2015], granular flows [Daviet and Bertails-Descoubes 2016], and snow [Stomakhin et al. 2013] have also seen much recent study, we focus on outstanding challenges in simulating the humble Newtonian viscous liquid, whose internal stresses are strictly linear with respect to the strain rate.

Standard grid-based fluid animation tools apply operator splitting to the incompressible Navier-Stokes equations to solve for the influence of advection, viscosity, and pressure in distinct stages [Bridson 2015]. While this splitting is effective at reducing computational cost, simplifying implementation, and isolating nonlinearity to the advection stage, it also introduces subtle sources of error. For example, separating advection from projection causes significant loss of kinetic energy and vorticity, making it more difficult to simulate turbulent, high Reynolds number flows [Mullen et al. 2009; Zhang and Bridson 2015].

Our work focuses on the opposite extreme: strongly viscous liquids, corresponding to moderate to low Reynolds numbers. We highlight a detrimental impact of splitting *viscosity* from projection that has gone largely unnoticed to date: behaviors that depend on coupling between pressure and shear forces are entirely absent, including preservation of sharp surface details and the remarkable

liquid rope coiling instability [Ribe et al. 2012] (Figure 1). Our key contribution is to replace the standard Eulerian viscosity and pressure steps with a novel *unsteady Stokes* step that reunites these forces and accurately recovers the missing effects of coupling.

A dominant source of error introduced by splitting is an improper treatment of the liquid's free surface. The correct boundary condition requires the interface to be traction-free, $\boldsymbol{t} = \sigma\boldsymbol{n} = 0$, where $\boldsymbol{t}$ is the surface traction, σ is the total fluid stress tensor, and $\boldsymbol{n}$ is the surface normal; simply put, the liquid surface should feel no resistance from the empty air side. Unfortunately, this condition *inherently* requires tight pressure-viscosity coupling, because fluid stress σ is a sum of pressure, p, and viscous shear stresses, τ, given by $\sigma = -p\boldsymbol{I} + \tau$.

Batty and Bridson [2008] simplified the traction-free condition by explicitly decoupling it into two *independent* boundary conditions: $p = 0$ for pressure, and $\tau\boldsymbol{n} = 0$ for viscosity. While this approach yielded improved results compared to earlier Laplacian smoothing-type viscosity models [Carlson et al. 2002; Rasmussen et al. 2004], including offering buckling effects and recovery of rigid body rotation, it is nevertheless a poor approximation: as Stomakhin et al. [2014] noted in adopting the same simplification, it is analogous to enforcing $a + b = 0$ by arbitrarily setting $a = 0$ and $b = 0$. We demonstrate that this error is responsible for loss of surface details and coiling effects in existing decoupled simulators, including that of Batty and Bridson [2008]; both issues can be seen in Figure 2.

Technical Contributions. We present a novel, unconditionally stable implicit unsteady Stokes solver to simultaneously apply pressure and viscous forces while enforcing the true free surface boundary conditions. Unlike steady-state Stokes solvers common in computational physics, which typically yield indefinite linear systems [Benzi et al. 2005; Elman 2002], we show how the unsteady (i.e., time-dependent) case can be exploited to yield a symmetric positive definite system. We discretize a carefully chosen variational form which allows the challenging free surface conditions to be enforced easily and implicitly as natural boundary conditions. We demonstrate that our method can be used as a drop-in replacement for the viscosity and pressure steps in standard fluid simulators by integrating it into Side Effects Software's Houdini [2016]. We present quantitative results supporting the method's accuracy, and qualitative results demonstrating its improved visual quality compared to standard approaches. In particular, our method recovers the classic rope coiling instability and preserves a higher degree of detail in viscous liquid surfaces, while maintaining support for familiar features such as moving boundaries and surface tension.

2 RELATED WORK

Grid-Based Viscous Liquid Animation. A brief review of the trajectory of grid-based viscous free surface liquids in computer animation shows a trend of steadily increasing physical accuracy, motivated by the pursuit of visual realism. Early work by Foster and Metaxas [1996] demonstrated an explicit discretization that is effective for relatively low viscosity liquids. Carlson et al. [2002] presented the first model focused on highly viscous liquids in graphics, proposing a treatment based on implicit componentwise Laplacian smoothing of velocity; however, it suffered from freezing in free

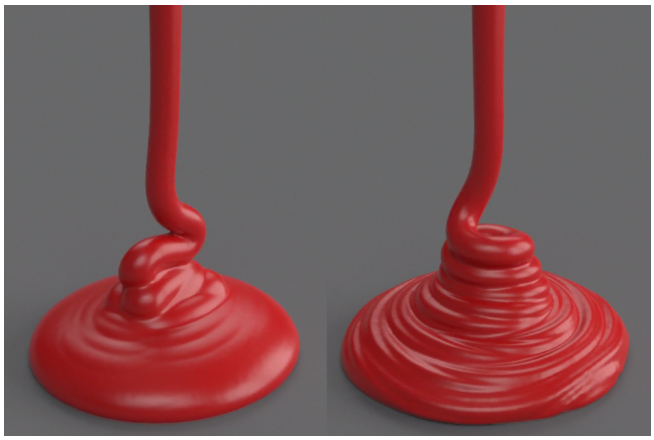

Fig. 2. Left: Standard approaches that decouple pressure and viscosity yield random buckling of a falling stream of viscous liquid. Right: Our unified Stokes approach yields the proper cylindrical coiling, and greater surface detail in the pile.

flight, likely due to inappropriate free surface boundary conditions. Soon after, Falt and Roble [2003] showed that a Neumann boundary condition of $\frac{\partial \boldsymbol{u}}{\partial \boldsymbol{n}} = 0$ gives correct translational motion. Rasmussen et al. [2004] pointed out that the Laplacian model neglects some cross-derivative terms of the fluid stresses when viscosity varies spatially, and proposed to integrate the missing terms explicitly.

Batty and Bridson [2008] observed that while the Neumann boundary conditions above allow translation of isolated bodies, they immediately destroy rotation, which in turn prevents viscous buckling effects. Noting that the surface boundary conditions should be traction-free to avoid unphysical ghost forces, they presented a fully implicit variational viscosity solver that naturally enforces the condition $\tau\boldsymbol{n} = 0$ (zero traction due to viscous shear stress), and is thereby able to recover some rotational effects. Batty and Houston [2011] later developed a spatially adaptive variant for Eulerian tetrahedral meshes. However, because these approaches still decouple pressure from viscosity, important errors remain and realistic coiling effects are not observed. Our work builds on the trend of gradually increasing physical accuracy by enforcing the full traction-free boundary condition, $\sigma\boldsymbol{n} = 0$, in a unified way.

Multiphase viscous liquids have been explored as well, typically by enforcing approximate jump conditions with decoupled viscosity and pressure at the fluid-fluid interface, using either a ghost fluid-type scheme [Hong and Kim 2005; Losasso et al. 2006] or volume fractions [Kang et al. 2010], similar to Batty and Bridson [2008].

Approaches in Computational Physics. Three-dimensional viscous liquids on regular grids have also been considered in computational physics. The GENSMAC scheme of Tomé et al. [2004; 1994] simulates a range of free surface phenomena, including coiling, by assuming that the surface normal is either aligned with or at a 45° angle to the coordinate axes, in order to tailor conditions for each special case. This effectively voxelizes the domain into a faceted stairstep approximation that poorly captures the smooth geometry, limiting the effectiveness of the approach and requiring a complex case-by-case implementation. The more stable implicit variant of their method relies on the bi-conjugate gradient method

to solve a non-symmetric linear system [Oishi et al. 2008]. Bonito et al. [2006] instead proposed a hybrid approach that uses a tetrahedral mesh to solve an indefinite finite element Stokes problem combined with grid-based advection. Sussman et al. [2007] presented a decoupled projection-based scheme for single- and two-phase flows that uses a semi-implicit discretization of viscous terms and a ghost-fluid-like interface treatment; they focus on bubbles and capillary effects rather than buckling or coiling. Recently, Lalanne et al. [2015] considered two-phase flows in two dimensions, and carried out a comparison of four different splitting techniques that consider the proper coupled interface conditions using ghost-fluid ideas, albeit still in a time-split (weakly coupled) fashion. The methods advocated by Lalanne et al. do not consider the free surface case where one fluid's density goes to zero, and must satisfy a stability criterion, in contrast to our unconditionally stable scheme. Another approach closely related to ours is that of Schroeder et al. [2014] who applied a finite-element-like variational formulation on a staggered cut-cell grid to solve Navier-Stokes problems with implicitly integrated viscosity and correct jump conditions for two-phase flow. While this method achieves greater accuracy, its discretization is substantially more complex than our weighted finite difference approach and it requires the solution of an indefinite linear system. The method does not handle scenarios where solid and air interfaces meet, and hence has not been applied to coiling or buckling phenomena.

Lagrangian Approaches. We focus on the Eulerian fluid paradigm, but a variety of purely Lagrangian approaches exist. Viscosity models for smoothed particle hydrodynamics (SPH) methods in graphics date back to the work of Desbrun and Gascuel [1996]. However, realistic buckling and coiling effects have only recently become the subject of substantial interest, with several groups proposing solutions [Andrade et al. 2015; Bender and Koschier 2016; Peer et al. 2015; Peer and Teschner 2016; Takahashi et al. 2015]. These methods vary in their faithfulness to the physical equations, but all take either an explicitly integrated or pressure-decoupled approach to viscosity, and none present quantitative evidence of accuracy.

Specialized Lagrangian approaches for slender viscous threads and sheets have been proposed [Batty et al. 2012; Bergou et al. 2010; Zhu et al. 2015, 2014] that extend ideas from rod and shell simulation. In particular, the viscous threads of Bergou et al. accurately reproduce both stationary coiling and the intricate patterns arising in a "fluid mechanical sewing machine" [Audoly et al. 2012; Brun et al. 2012]. Their efficiency and accuracy comes at the cost of generality, however: lower-dimensional methods cannot easily be used for general volumetric flows.

The viscous free surface condition has not been studied closely in conforming Lagrangian tetrahedral mesh methods (e.g., [Clausen et al. 2013; Misztal et al. 2012]), although these methods should incorporate it implicitly. However, such methods are less attractive from a practical standpoint: robust continuous tetrahedral remeshing is computationally expensive and challenging to implement, whereas the regular structure of uniform grids readily offers high performance (e.g., [Setaluri et al. 2014]). This fact largely accounts for the dominance of grid-based methods in industry. Furthermore, these methods have so far led to symmetric *indefinite* linear systems, in contrast to our *positive definite* formulation.

Positive Definite Stokes Flow. Robinson-Mosher et al. [2011] developed a similar symmetric positive definite formulation of unsteady Stokes flow for solid-fluid coupling. However, their viscosity discretization uses voxelized solid geometry and spatially constant viscosity, and does not support free surfaces. Moreover, our derivation identifies their purely algebraic transformation as a change of variables from a velocity-pressure formulation to a pressure-stress formulation, lending physical insight and exposing a fundamental variational expression of the mechanics.

Embedded Boundary Methods. Our work is an instance of an embedded boundary method, which is a family of techniques that account for irregular geometry while nevertheless using an underlying uniform regular grid. Our method can be considered a unification of several existing embedded discretizations: the ghost fluid free surface pressure projection of Enright et al. [2003], the variational solid pressure projection of Batty et al. [2007] and Ng et al. [2009], and the viscous free surface scheme of Batty and Bridson [2008].

Variational Discretizations. We use a variational formulation that leads to a backward Euler time integration scheme, a perspective that has also been applied to elastic solids [Gast et al. 2015], tetrahedral fluids [Erleben et al. 2011; Misztal et al. 2010], grid-based fluids [Batty et al. 2007; Batty and Bridson 2008], and fluid and solid control [Martin et al. 2011; Nielsen and Christensen 2010].

Grid-Based Non-Newtonian Flows. There are several techniques that rely (at least partly) on Eulerian regular grids to treat elastic, elastoplastic, and non-Newtonian materials involving *nonlinear* constitutive laws, including material point methods (MPM) and Eulerian solids [Goktekin et al. 2004; Levin et al. 2011; Ram et al. 2015; Stomakhin et al. 2013, 2014; Yue et al. 2015]. These materials generally require linearization or more expensive iterative solvers, such as Newton's method, to circumvent or address nonlinearity. On the other hand, since Rayleigh damping of an elastic body is equivalent to Newtonian fluid viscosity under appropriate conditions [Batty et al. 2012; Bergou et al. 2010], these methods could (in principle) be adapted for purely viscous fluids. However, beyond treatment of nonlinearity there are several reasons that we instead propose a tailored Stokes solver for Newtonian fluids. First, (visco-)elastic models often assume a moderate to high degree of compressibility, and struggle in the limit of incompressibility; while some authors have considered this explicitly [Goktekin et al. 2004; Stomakhin et al. 2014], they do so using a splitting that once again decouples pressure and viscosity. Second, the quadratic or cubic shape functions often used in MPM lead to denser linear systems, in contrast to our finite difference approach. Third, these methods do not generally account for the sub-grid position of the interface, instead relying on voxelization that can lead to stairstep artifacts in fluids [Batty et al. 2007; Enright et al. 2003]. Lastly, existing semi-implicit viscoelastic MPM discretizations lead to potentially indefinite systems [Stomakhin et al. 2013, 2014] (or even nonsymmetric systems in the presence of plasticity [Klar et al. 2016]), requiring sub-optimal solvers such as MINRES or GMRES. By contrast we can guarantee a symmetric positive definite system.

3 FLUID EQUATIONS

The incompressible Navier-Stokes equations [Batchelor 1967] are

$$\frac{\partial \boldsymbol{u}}{\partial t} = -\boldsymbol{u} \cdot \nabla \boldsymbol{u} - \frac{\nabla p}{\rho} + \frac{\nabla \cdot \tau}{\rho} + \frac{\boldsymbol{f}}{\rho}, \tag{1}$$

$$\nabla \cdot \boldsymbol{u} = 0, \tag{2}$$

$$\tau = \mu \left(\nabla \boldsymbol{u} + (\nabla \boldsymbol{u})^{\top} \right), \tag{3}$$

where ρ is density, $\boldsymbol{u}$ is velocity, p is pressure, τ is the symmetric deviatoric stress tensor, μ is the dynamic viscosity coefficient, t is time, and $\boldsymbol{f}$ is external forces. We allow μ to vary smoothly in space.

Time Discretization. We apply operator splitting and discretize in time, yielding a two step scheme. Advection and external forces are treated first by solving

$$\frac{\boldsymbol{u}^* - \boldsymbol{u}_n}{\Delta t} = -\boldsymbol{u}_n \cdot \nabla \boldsymbol{u}_n + \frac{\boldsymbol{f}}{\rho} \tag{4}$$

to arrive at an intermediate velocity $\boldsymbol{u}^*$, where $\boldsymbol{u}_n$ is the velocity at time step n, and Δt is the time step. Our method is agnostic as to the choice of advection technique; our simulations use the affine particle-in-cell (APIC) approach [Jiang et al. 2015], but we observed comparable results with semi-Lagrangian and FLIP schemes.

We then simultaneously integrate pressure and viscous forces using backward Euler by solving

$$\frac{\boldsymbol{u}_{n+1} - \boldsymbol{u}^*}{\Delta t} = \frac{1}{\rho} \left(-\nabla p + \nabla \cdot \tau \right), \tag{5}$$

$$\nabla \cdot \boldsymbol{u}_{n+1} = 0, \tag{6}$$

$$\tau = \mu \left(\nabla \boldsymbol{u}_{n+1} + (\nabla \boldsymbol{u}_{n+1})^{\top} \right). \tag{7}$$

These are the equations for a fully implicit step of time-dependent or *unsteady Stokes flow*, allowing for spatially varying viscosity. Our contribution is a new solver for this PDE.

These equations should be contrasted with *steady-state* Stokes flow, in which the left side of (5) becomes zero. Such a simplification applies only to creeping flows in which viscous forces dominate and inertia is negligible; it is inappropriate for use with the Navier-Stokes equations across wider ranges of viscosity.

Boundary Conditions. The solid boundary condition is no-slip: the new fluid velocity $\boldsymbol{u}_{n+1}$ should match the boundary velocity, $\boldsymbol{u}_{\text{BC}}$, giving $\boldsymbol{u}_{n+1} = \boldsymbol{u}_{\text{BC}}$. The free surface condition states that the traction $\boldsymbol{t}$ must match the desired traction $\boldsymbol{t}_{\text{BC}}$

$$\boldsymbol{t} = \sigma \boldsymbol{n} = (-p\boldsymbol{I} + \tau)\boldsymbol{n} = \boldsymbol{t}_{\text{BC}}. \tag{8}$$

Here $\boldsymbol{n}$ is the outward unit normal of the free surface, and $\boldsymbol{I}$ is the identity tensor. Without surface tension, $\boldsymbol{t}_{\text{BC}} = \boldsymbol{0}$ ensuring the absence of artificial ghost forces from the empty "air" side of the interface. Adding surface tension gives $\boldsymbol{t}_{\text{BC}} = \gamma \kappa \boldsymbol{n}$, where γ is the coefficient of surface tension and κ is the curvature at the surface.

4 VARIATIONAL FORMULATIONS

For staggered grid finite difference schemes based on directly discretizing the above PDE form, it is difficult to derive appropriate discrete boundary conditions for non-grid-aligned boundaries, especially for free surfaces. We address this by instead using a variational framework that handles irregular geometry through natural boundary conditions, building on work by Batty et al. [2007; 2008].

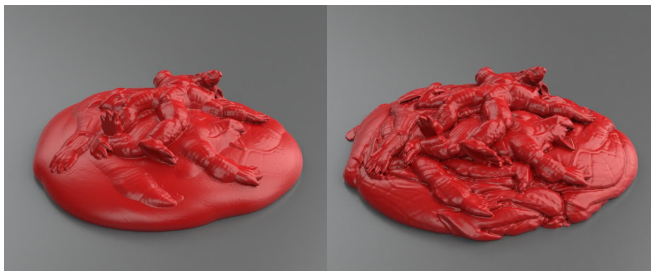

Fig. 3. Collapsed piles of viscous armadillos. Left: The incorrect boundary conditions of the standard decoupled solve lead to rapid loss of surface detail. Right: Our Stokes solver with correct traction-free surfaces better preserves fine details of the armadillos.

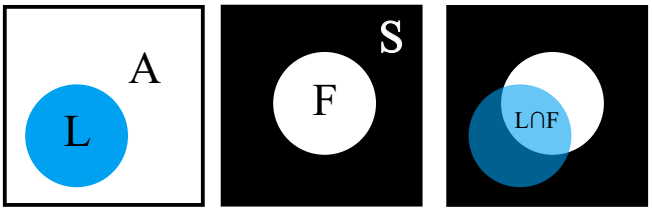

Fig. 4. Left: Liquid vs. air domains for free surface case. Middle: Fluid vs. solid domains for solid boundary case. Right: For scenarios with both free surface and solid boundaries, the active region is the intersection of the liquid and fluid regions.

We will initially consider the free surface and solid boundary cases separately. In the free surface case, an interface separates a massless air region Ω_A from the active liquid region Ω_L (Figure 4, left). In the solid case, we distinguish the active fluid region Ω_F from the surrounding prescribed solid region Ω_S (Figure 4, middle). These boundaries will be represented as level sets. When considering both types of boundary conditions, the active region will be the *intersection* of "liquid" (non-air) and "fluid" (non-solid) regions, $\Omega_L \cap \Omega_F$ (Figure 4, right). In a simulation, the liquid region "inside" the solid wall is constructed by extending the liquid level set in the solid's normal direction.

Free Surface Case. A variational formulation of our unsteady Stokes problem with free surfaces boundaries is

$$\max_{p,\tau} \min_{\boldsymbol{u}_{n+1}} \iiint_{\Omega_L} \frac{\rho}{2} \|\boldsymbol{u}_{n+1} - \boldsymbol{u}^*\|^2 - \Delta t p \nabla \cdot \boldsymbol{u}_{n+1} + \Delta t \tau : \left(\frac{\nabla \boldsymbol{u}_{n+1} + (\nabla \boldsymbol{u}_{n+1})^{\top}}{2} \right) - \frac{\Delta t}{4\mu} \|\tau\|_F^2 \, dV. \tag{9}$$

where $\| \cdot \|_F$ is the Frobenius norm and ':' indicates a tensor double dot product. The domain of integration is the liquid (i.e., non-air) region, Ω_L. In the supplemental material, we prove that the optimality conditions are exactly the original PDE, with the free surface condition (8) with $\boldsymbol{t}_{\text{BC}} = \boldsymbol{0}$ enforced as a natural boundary condition. Consequently, assuming the necessary integrals are discretized appropriately, the free surface condition will be handled automatically, including the coupling between pressures and viscous stresses that is absent in previous methods. (Discarding the pressure terms recovers an equivalent of the decoupled viscosity formulation of

Batty and Bridson [2008]. Discarding the viscous stress terms gives a variational form of the ghost fluid method [Enright et al. 2003].)

Solid Case. A variational formulation of unsteady Stokes with static solid boundaries is

$$\max_{p,\tau}\min_{\boldsymbol{u}_{n+1}} \iiint_{\Omega_F} \frac{\rho}{2}\|\boldsymbol{u}_{n+1}-\boldsymbol{u}^*\|^2 + \Delta t\boldsymbol{u}_{n+1}\cdot(\nabla p-\nabla\cdot\tau)-\frac{\Delta t}{4\mu}\|\tau\|_F^2\,dV. \tag{10}$$

Here the integration is performed over the fluid (i.e., non-solid) region, Ω_F. (Discarding the terms involving stress essentially recovers an alternate form of the variational pressure projection of Batty et al. [2007] for static solids.)

The solid and free surface forms above differ by integration by parts on the middle terms, except the resulting boundary integral term is discarded. In essence, this is what "switches" the natural boundary condition from free surface to solid. Unfortunately, at the continuous level we cannot simultaneously have *both* solid and free surface conditions enforced naturally, without extra boundary integral terms that are difficult to discretize consistently. However, we will demonstrate that combining these two formulations at the discrete level is straightforward and effective.

4.1 Non-Zero Boundary Conditions

The preceding formulations yield *homogeneous* (zero) boundary conditions, yet we often need non-zero boundary conditions. Non-zero boundary velocities are used for moving solids and inflow/outflow boundaries; non-zero pressure (surface traction) conditions are used for surface tension. We can treat these cases by adding new terms that account for the *work* done at the boundary.

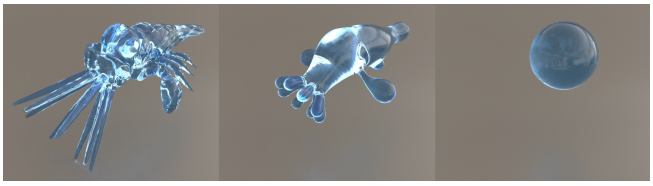

Fig. 5. Our method supports surface tension effects, which cause this liquid Houdini Squab in zero gravity to collapse into a sphere.

Prescribed Traction Boundaries. The work done by the prescribed traction at the surface is given by

$$\iint_{\partial\Omega_A} \Delta t\boldsymbol{u}_{n+1}\cdot(p_{\text{BC}}\boldsymbol{I}-\tau_{\text{BC}})\boldsymbol{n}\,dA, \tag{11}$$

where p_{BC} and τ_{BC} are the prescribed pressure and deviatoric stress, respectively, and $\boldsymbol{n}$ is the outward unit normal with respect to the air (non-liquid) region, Ω_A. We add this term to (9). (Only the resulting normal component of the stress, i.e., traction, will be enforced.) For consistency with the volume integral formulation, and to avoid discretizing surface quantities, we convert this surface integral into a volume integral via integration by parts, giving

$$\Delta t\iiint_{\Omega_A}\left(p_{\text{BC}}\nabla\cdot\boldsymbol{u}_{n+1}-\tau_{\text{BC}}:\left(\frac{\nabla\boldsymbol{u}_{n+1}+(\nabla\boldsymbol{u}_{n+1})^\top}{2}\right) + \boldsymbol{u}_{n+1}\cdot(\nabla p_{\text{BC}}-\nabla\cdot\tau_{\text{BC}})\right)dV. \tag{12}$$

Prescribed Velocity Boundaries. The work done at the moving solid boundary is similarly given by

$$\iint_{\partial\Omega_S}\Delta t\boldsymbol{u}_{\text{BC}}\cdot(p\boldsymbol{I}-\tau)\boldsymbol{n}\,dA, \tag{13}$$

where $\boldsymbol{n}$ is the outward unit normal to the solid region, Ω_S. We add this term to (10). Transforming to volume integral form we have

$$\Delta t\iiint_{\Omega_S}\left(p\nabla\cdot\boldsymbol{u}_{\text{BC}}-\tau:\left(\frac{\nabla\boldsymbol{u}_{\text{BC}}+(\nabla\boldsymbol{u}_{\text{BC}})^\top}{2}\right) + \boldsymbol{u}_{\text{BC}}\cdot(\nabla p-\nabla\cdot\tau)\right)dV. \tag{14}$$

5 DISCRETIZATION

Given a particular variational formulation, we can discretize the required integrals on a staggered grid following the *variational finite difference* framework of Batty et al. [2007; 2008]. While a finite element method (FEM) could be used instead, our approach is quite simple and convergent, reduces to a direct staggered finite difference discretization on interior cells, avoids the need for a boundary-conforming mesh, and does not require stabilization.

Staggered Grid Layout. We discretize the derivatives using centered finite differences, with pressures at cell centers and velocity components on cell faces. To support viscosity we also need the components of the deviatoric stress tensor. The most natural placement is diagonal components of the stress tensor $(\tau_{xx},\tau_{yy},\tau_{zz})$ at cell centers, and off-diagonal components $(\tau_{xy},\tau_{xz},\tau_{yz})$ on cell edges (cell corners in two dimensions); see Figures 6a and 6b. Since τ is symmetric, these six components suffice. Straightforward centered differencing then places the required derivatives in the correct locations. This layout was initially proposed in computational physics [Darwish et al. 1992; Mompean and Deville 1997], and first used in graphics by Goktekin et al. [2004] for viscoelastic fluids.

Integral Approximations and Control Volumes. We approximate the volume integrals by scaling each discretized term by the fractional volume of material in a cell-sized control volume surrounding the relevant sample point (cell center, edge midpoint, or face center), and summing over all cells.

For the free surface boundary problem, we need the volume fractions interior to the liquid (i.e., not air) region, which we gather into diagonal matrices denoted W_L. Later, we will also need the corresponding air fractions, $W_A=(\Delta x)^3I-W_L$, where I is the identity. Likewise, for the solid problem, we estimate the volume fractions W_F of each cell that are inside the fluid (i.e., not solid) region, and its complementary solid fraction, $W_S=(\Delta x)^3I-W_F$. These volume fractions are readily estimated from a level set representation (e.g., [Min and Gibou 2007]).

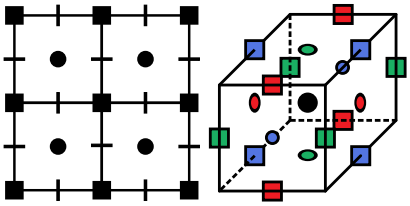

(a) (b)

Fig. 6. Left: Staggered pressure-velocity-stress grid layout in 2D. Black disks indicate pressure (p) and diagonal stress components (τ_{xx}, τ_{yy}). Dashes on cell faces indicate velocity components. Nodal black squares indicate off-diagonal stress components (τ_{xy}). Right: Staggered pressure-velocity-stress grid layout in 3D. The central black disk indicates pressure (p) and diagonal stress components (τ_{xx}, τ_{yy}, τ_{zz}). The colored squares on cell edges indicate off-diagonal stress components (τ_{yz} is red, τ_{xz} is green, τ_{xy} is blue). Colored circles on cell faces indicate velocity components (u is red, v is green, w is blue).

Discrete Free Surface Problem. The integral in (9) is over the liquid domain, Ω_L, so we use volume weights with subscript L. The first term consists of velocity data which lies on faces, so we estimate the integral using the face-centered volume weights. We use superscripts on the weights to indicate the control volume type, so in this case the weights are W_L^u. The second term involves pressures and divergences at cell centers, so we use cell-centered weights, W_L^p. The last two terms involves stresses on cell edges and centers, so the weights are W_L^τ.

This leads to the following discrete Stokes problem with (only) free surface boundaries:

$$\max_{\mathbf{p},\boldsymbol{\tau}} \min_{\mathbf{u}} \frac{1}{2}(\mathbf{u}-\mathbf{u}^*)^\top \mathbf{P} W_L^u (\mathbf{u}-\mathbf{u}^*) + \Delta t \mathbf{p}^\top W_L^p \mathbf{G}^\top \mathbf{u} + \Delta t \boldsymbol{\tau}^\top W_L^\tau \mathbf{D}\mathbf{u} - \frac{\Delta t}{4} \boldsymbol{\tau}^\top \mathbf{M}^{-1} W_L^\tau \boldsymbol{\tau}. \tag{15}$$

In this expression $\mathbf{u}$, $\boldsymbol{\tau}$ and $\mathbf{p}$ are the stacked velocity components, stress components and pressures respectively, $\mathbf{P}$ is a diagonal matrix of densities per velocity sample, $\mathbf{M}$ is a diagonal matrix of viscosity coefficients per stress sample, $\mathbf{G}$ is the usual discrete gradient operator for pressure, and $\mathbf{D}$ is the discrete deformation rate operator for velocity (ie. $\mathbf{D}\mathbf{u} \approx \frac{1}{2}(\nabla \boldsymbol{u} + (\nabla \boldsymbol{u})^\top)$). The negative transposes of $\mathbf{G}$ and $\mathbf{D}$ correspond to discrete vector and tensor divergence operators up to scaling, respectively.

The optimality conditions of this quadratic problem yield the following symmetric indefinite linear system:

$$\begin{pmatrix} \frac{1}{\Delta t}\mathbf{P}W_L^u & \mathbf{D}^\top W_L^\tau & \mathbf{G}W_L^p \\ W_L^\tau \mathbf{D} & -\frac{1}{2}\mathbf{M}^{-1}W_L^\tau & 0 \\ W_L^p \mathbf{G}^\top & 0 & 0 \end{pmatrix} \begin{pmatrix} \mathbf{u} \\ \boldsymbol{\tau} \\ \mathbf{p} \end{pmatrix} = \begin{pmatrix} \frac{1}{\Delta t}\mathbf{P}W_L^u \mathbf{u}^* \\ 0 \\ 0 \end{pmatrix}. \tag{16}$$

Discrete Solid Boundary Problem. The solid boundary problem (10) is discretized in the same way, except using the fluid (non-solid) volume fraction weights W_F instead. The discrete form is

$$\max_{\mathbf{p},\boldsymbol{\tau}} \min_{\mathbf{u}} \frac{1}{2}(\mathbf{u}-\mathbf{u}^*)^\top \mathbf{P} W_F^u (\mathbf{u}-\mathbf{u}^*) + \Delta t \mathbf{u}^\top W_F^u (\mathbf{G}\mathbf{p} + \mathbf{D}^\top \boldsymbol{\tau}) - \frac{\Delta t}{4} \boldsymbol{\tau}^\top \mathbf{M}^{-1} W_F^\tau \boldsymbol{\tau}. \tag{17}$$

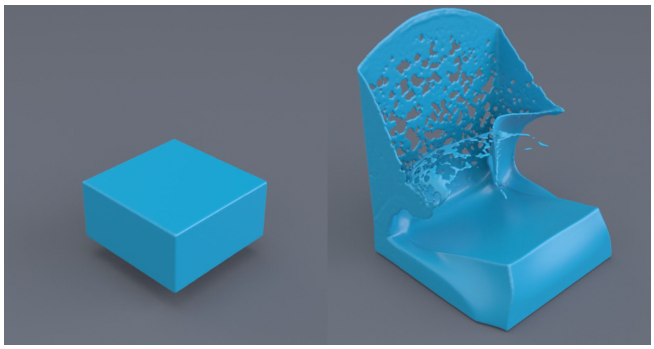

Fig. 7. Left: A block of liquid with spatially varying viscosity is dropped. Right: The low viscosity end splashes dramatically, while the high viscosity end deforms gently.

The linear system for the static solid wall Stokes problem is

$$\begin{pmatrix} \frac{1}{\Delta t}\mathbf{P}W_F^u & W_F^u \mathbf{D}^\top & W_F^u \mathbf{G} \\ \mathbf{D}W_F^u & -\frac{1}{2}\mathbf{M}^{-1}W_F^\tau & 0 \\ \mathbf{G}^\top W_F^u & 0 & 0 \end{pmatrix} \begin{pmatrix} \mathbf{u} \\ \boldsymbol{\tau} \\ \mathbf{p} \end{pmatrix} = \begin{pmatrix} \frac{1}{\Delta t}\mathbf{P}W_F^u \mathbf{u}^* \\ 0 \\ 0 \end{pmatrix}. \tag{18}$$

Combined Discrete Problem. Because these two systems have nearly identical forms, and differ only by the weighting matrices W that implicitly enforce boundaries, we can combine them to handle both free surfaces and solids in the same problem by simply using both diagonal weight matrices together:

$$\begin{pmatrix} \frac{1}{\Delta t}\mathbf{P}W_F^u W_L^u & W_F^u \mathbf{D}^\top W_L^\tau & W_F^u \mathbf{G} W_L^p \\ W_L^\tau \mathbf{D} W_F^u & -\frac{1}{2}\mathbf{M}^{-1}W_F^\tau W_L^\tau & 0 \\ W_L^p \mathbf{G}^\top W_F^u & 0 & 0 \end{pmatrix} \begin{pmatrix} \mathbf{u} \\ \boldsymbol{\tau} \\ \mathbf{p} \end{pmatrix} = \begin{pmatrix} \frac{1}{\Delta t}\mathbf{P}W_F^u W_L^u \mathbf{u}^* \\ 0 \\ 0 \end{pmatrix}. \tag{19}$$

Combining the two formulations at the discrete level lets us exploit the natural conditions for both boundary types simultaneously. If one considers boundary regions away from triple curves (i.e., where liquid meets both solid and air), the weights ensure that this combined system simply reduces back to the system for the appropriate boundary condition, while triple curves also behave naturally. We further verified that this approach gives the expected zero velocity fields for triple curves in hydrostatic scenarios. (Batty et al. [2008] used a similar approach to combine variational Neumann boundary conditions with ghost fluid-based Dirichlet conditions.)

Transformation to Positive Definite Form. The system above is sparse, symmetric *indefinite*, and large since it involves three variables: pressure, stress, and velocity. Eliminating *stress* by applying a Schur complement to the center block would yield a symmetric indefinite velocity-pressure system of a form most commonly associated with (steady) Stokes problems [Benzi et al. 2005; Robinson-Mosher et al. 2009, 2008].

One typically prefers *symmetric positive-definite* (SPD) systems, as they are more amenable to efficient techniques such as preconditioned conjugate gradient, domain decomposition, multigrid, etc. We transform to an SPD form by noting that the upper-left block is

diagonal; i.e., trivially invertible. This lets us find the Schur complement of this block, eliminating *velocity* instead of stress, to arrive at a smaller SPD system for pressure and stress.

The resulting SPD pressure-stress form of (19) is

$$\begin{pmatrix} \mathbf{A}_{11} & \mathbf{A}_{12} \\ \mathbf{A}_{12}^\top & \mathbf{A}_{22} \end{pmatrix} \begin{pmatrix} \boldsymbol{\tau} \\ \mathbf{p} \end{pmatrix} = \begin{pmatrix} W_L^\tau \mathbf{D} W_F^u \mathbf{u}^* \\ W_L^p \mathbf{G}^\top W_F^u \mathbf{u}^* \end{pmatrix} \tag{20}$$

where the blocks of the matrix are given by

$$\begin{aligned} \mathbf{A}_{11} &= \frac{1}{2}\mathbf{M}^{-1} W_L^\tau W_F^\tau + \Delta t W_L^\tau \mathbf{D} \mathbf{P}^{-1} W_L^{u\,-1} W_F^u \mathbf{D}^\top W_L^\tau, \\ \mathbf{A}_{12} &= \Delta t W_L^\tau \mathbf{D} \mathbf{P}^{-1} W_L^{u\,-1} W_F^u \mathbf{G} W_L^p, \\ \mathbf{A}_{22} &= \Delta t W_L^p \mathbf{G}^\top \mathbf{P}^{-1} W_L^{u\,-1} W_F^u \mathbf{G} W_L^p. \end{aligned} \tag{21}$$

Close inspection reveals that this is identical to a direct finite difference discretization of (5)-(7) where velocity has been eliminated by plugging (5) into (6) and (7), except that volume fraction weight terms have been added to implicitly handle boundaries.

A similar SPD transformation was proposed by Robinson-Mosher et al. [2011], albeit for constant Laplacian-based viscosity with grid-aligned boundaries and no free surfaces. Analogous transformations are of course common for articulated rigid bodies and other constrained dynamics problems (e.g., [Baraff 1996; Goldenthal et al. 2007; Tournier et al. 2015]).

5.1 Discretized Non-Zero Boundary Conditions

Prescribed Traction Boundaries. Using W_A terms to indicate the air fraction of a control volume, the discretized form of (12) is

$$\Delta t \left(\mathbf{u}^\top W_A^u (\mathbf{G}\mathbf{p}_{\text{BC}} + \mathbf{D}^\top \boldsymbol{\tau}_{\text{BC}}) - \mathbf{p}_{\text{BC}}^\top W_A^p \mathbf{G}^\top \mathbf{u} - \boldsymbol{\tau}_{\text{BC}}^\top W_A^\tau \mathbf{D}\mathbf{u} \right), \tag{22}$$

which results in added terms on the right hand side of (20):

$$\begin{pmatrix} \Delta t W_L^\tau \mathbf{D} W_F^u \mathbf{P}^{-1} \mathbf{g}_{\text{BC}} \\ \Delta t W_L^p \mathbf{G}^\top W_F^u \mathbf{P}^{-1} \mathbf{g}_{\text{BC}} \end{pmatrix}, \tag{23}$$

where $\mathbf{g}_{\text{BC}} = (\mathbf{G} W_A^p - W_A^u \mathbf{G})\mathbf{p}_{\text{BC}} + (\mathbf{D}^\top W_A^\tau - W_A^u \mathbf{D}^\top)\boldsymbol{\tau}_{\text{BC}}$. Additionally, we must also add $\Delta t W_L^{u\,-1} \mathbf{P}^{-1} \mathbf{g}_{\text{BC}}$ to the velocity update. We can use this mechanism to apply arbitrary tractions, including surface tension. However, in practice we found that for surface tension an approach closer in form to ghost fluid [Enright et al. 2003] gives improved results with less drift for high viscosity and surface tension coefficients. This is achieved by rounding the W_A^p entries in (23) to the nearest cell volume: Δx^3 if the cell is more than half full, and 0 otherwise. This form still differs slightly from true ghost fluid, in that we use volume rather than length fractions for W_L^u, but this choice is fairly common (e.g.,[Narain et al. 2008]) and has no visible impact on the result.

While the air domain extends far from the liquid surface, only contributions near the surface actually play a role in the linear system and affect the results.

Prescribed Velocity Boundaries. Using solid fractions W_S and discretizing (14) as usual, we arrive at the expression

$$\Delta t \left(\mathbf{u}_{\text{BC}}^\top W_S^u (\mathbf{G}\mathbf{p} + \mathbf{D}^\top \boldsymbol{\tau}) - \mathbf{p}^\top W_S^p \mathbf{G}^\top \mathbf{u}_{\text{BC}} - \boldsymbol{\tau}^\top W_S^\tau \mathbf{D}\mathbf{u}_{\text{BC}} \right). \tag{24}$$

This results in additional terms on the right hand side of (20), namely

$$\begin{pmatrix} W_L^\tau \mathbf{D} W_S^u \mathbf{u}_{\text{BC}} - W_L^\tau W_S^\tau \mathbf{D}\mathbf{u}_{\text{BC}} \\ W_L^p \mathbf{G}^\top W_S^u \mathbf{u}_{\text{BC}} - W_L^p W_S^p \mathbf{G}^\top \mathbf{u}_{\text{BC}} \end{pmatrix}. \tag{25}$$

For non-zero solid boundary velocities, our initial velocity vector $\mathbf{u}^*$ must also include the boundary velocities. No additional steps are needed when updating velocities after the solve.

5.2 Stress Reduction

A property of the fluid stress tensor can let us eliminate one more variable to further shrink the system size. Because pressure enforces incompressibility, $\nabla \cdot \boldsymbol{u} = 0$, it must also be true that $\text{Tr}\left(\nabla \boldsymbol{u} + (\nabla \boldsymbol{u})^\top\right) = 0$. Since the deviatoric stress τ is defined as $\tau = \mu\left(\nabla \boldsymbol{u} + (\nabla \boldsymbol{u})^\top\right)$, it will also be traceless, consistent with its physical definition. Therefore we can eliminate one of its diagonal elements without loss of information. Specifically, in 2D we have $\text{Tr}(\tau) = \tau_{xx} + \tau_{yy} = 0$, so we can substitute $\tau_{yy} = -\tau_{xx}$ into our system to eliminate τ_{yy}, recovering it after the solve if needed. In 3D we similarly substitute $\tau_{zz} = -(\tau_{xx} + \tau_{yy})$. Symmetry of the linear system is nevertheless preserved. Our implementation makes use of this extra reduction, applied at the discrete level.

5.3 Null Space Elimination

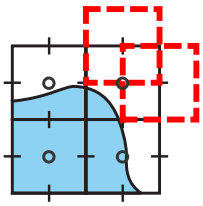

A final remaining issue is the occurrence of null spaces due to overlapping volume weights assigned to different terms of the discrete variational problem. For example, consider the divergence operator for a cell near a free surface boundary. There are volume weights associated with both velocities (face centers) and pressures (cell centers), and cases often arise in which a pressure cell with a non-zero associated liquid volume weight enforces a divergence constraint involving at least one velocity face with zero associated liquid volume. Zero-weighted velocity samples play no role in other equations, and may take on any values as long as they satisfy the cell's constraint.

Only degrees of freedom with positive volume weights are used to update the simulation afterwards, so the physical solution is not damaged by null spaces. However, they do hamper the efficiency of iterative solvers, so we prefer to eliminate them. To do so, we identify each variable that enforces a relationship on a degree of freedom with a zero volume weight; e.g., in the free surface example above a non-zero weighted pressure is tagged as invalid if it enforces the divergence-free condition on one or more velocity faces with zero weights. Likewise in the solid boundary case, if a non-zero weighted velocity sample borders a zero-weighted pressure sample, that velocity sample is tagged as invalid and its corresponding equation(s) eliminated. This process is likewise extended to viscous terms. The reduced set of equations retains symmetry and has the same solution (for positively weighted variables), but no longer suffers from large null spaces. As for standard pressure projection, a single one-dimensional null space remains for completely enclosed fluid domains without a free surface. As usual, it can be removed by arbitrarily fixing the pressure of one fluid cell provided that any right-hand-side components in the null space have been projected out to ensure compatibility.

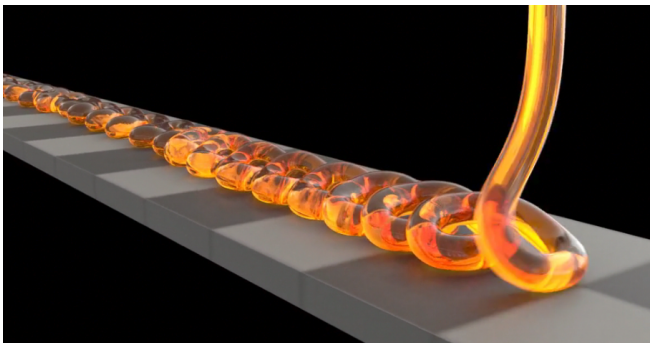

Fig. 8. A stream of liquid coiling onto a moving conveyor belt.

6 RESULTS

We implemented our method inside Houdini's [Side Effects Software 2016] fluid simulator, replacing the pressure and viscosity steps with our Stokes solver. This let us compare against an industrial solver with no algorithmic differences beyond our core contribution. Houdini's viscosity solver is an implementation of the decoupled variational approach of Batty and Bridson [2008]. To verify that its observed lack of coiling is due to the earlier method itself, rather than an implementation error, we independently reimplemented the method from scratch; our supplemental video demonstrates that this code gives results consistent with Houdini's, and does not coil. Our code will be made available online as a plugin for Houdini 16.

6.1 Animation Examples

Rope Coiling. Figure 1 shows our method reproducing the liquid rope coiling instability [Ribe et al. 2012] of a stream of falling honey. Figure 2 shows a comparison of Houdini's decoupled approach against our method, demonstrating that only the latter successfully produces coiling; it also preserves greater surface detail due to the proper coupling between pressure and viscous stresses in the free surface boundary condition. Our video also shows the same scenario with stronger viscosity, leading to a larger coiling radius, while the decoupled approach again buckles randomly. Although our method preserves more surface detail, if physical smoothing *is* desired we can add surface tension, while retaining greater control over the smoothing rate than is possible with the decoupled approach. We demonstrate this with a coiling molasses example with stronger surface tension (inset figure). Figure 8 shows a stream of viscous liquid coiling as it is poured onto a moving conveyor belt.

Piling Armadillos. In Figure 3 we have dropped nine copies of the Stanford armadillo with random orientations into a pile. While the coarse-scale behavior is similar between the decoupled and Stokes approaches, the surface in the former case "relaxes" very quickly, while the our method again preserves much more surface detail due to the accurate free surface conditions.

Colliding Characters. Our unified solve ensures that the velocities remain on the manifold of incompressible vector fields at the same time as viscous forces are integrated. This allows energy to be transferred more accurately among translation, rotation, and deformation modes of liquid bodies. By contrast, a decoupled solve causes more energy to be projected away whenever the viscous solve produces intermediate velocity fields with large divergence. This often manifests as stiffer viscous deformation or lost momentum. To demonstrate, we collide two viscous characters and observe that the resulting rate of rotation is faster with Stokes (Figure 9). From an aesthetic perspective, the Stokes simulator tends to produce slightly more lively (i.e., less stiff) simulations than a decoupled solver for the same parameter settings.

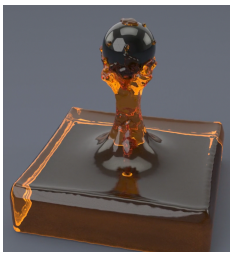

Ball Through Goop. We demonstrate our support for moving boundaries with a solid sphere passing up through a rectangular volume of viscous orange goo. As the inset figure shows, the no-slip condition causes the sphere to drag a stream of the liquid up into the air with it.

Collapsing Liquid Squab. To show that our method is effective in more general surface tension-dominated scenarios, we apply it to Houdini's Squab character model in zero gravity (Figure 5). Its various limbs quickly pull inwards as it seeks to reduce surface area.

Variable Viscosity Block. Figure 7 illustrates spatially varying viscosity by reproducing an example of Batty and Bridson [2008]. We drop a block of liquid with viscosity varying along its length, causing it to splash at one end and warp slightly at the other.

Caramel on Wafer. To demonstrate that we also still retain support for the smooth buckling effects exhibited by the decoupled method, we animate a layer of caramel folding onto a chocolate bar wafer in Figure 11. We approximate cooling by increasing viscosity gradually over time along the bar.

6.2 Convergence Studies

We have verified that our solver computes exact solutions, up to numerical precision, for time-dependent Stokes problems with linear solutions on irregular (i.e., non-grid-aligned) domains. This includes the case of hydrostatic fluid with solid (and possibly free surface) boundaries, as well as rigid translations and rotations of liquid bodies with pure free surface boundaries.

To further validate the accuracy of our method we performed a refinement study on a pair of more difficult problems (one with free surface, one with solid boundary) in two dimensions, comparing against their analytical solutions. Both involve curved non-grid-aligned boundaries, and we consider a single time step. A log-log plot of the L_∞ velocity error against the grid resolution is shown in Figure 10, indicating first order convergence in space for velocity. Further details are provided in the supplemental material.

We emphasize that while authors in graphics often refer to the ghost fluid method for free surfaces [Enright et al. 2003] and cut-cell scheme for solids [Ng et al. 2009] as second order accurate, this refers to the *pressure* variable; the velocity variable is only first order accurate, which matches our results. Moreover, the crucial issue for visual purposes is that the surface be free of grid-dependent stairstep artifacts; this is clearly the case for our results.

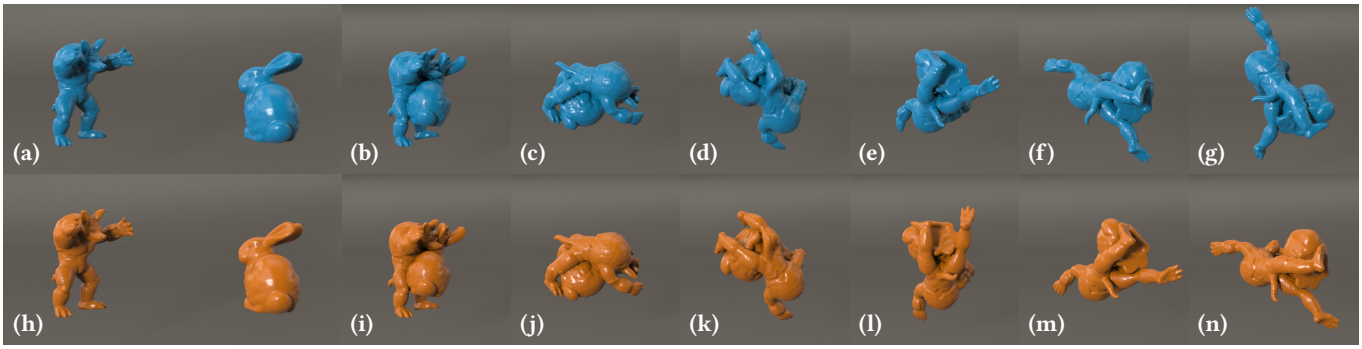

Fig. 9. Collision of a bunny and armadillo in zero gravity. Top row: Our Stokes method in blue. Bottom row: The decoupled viscosity scheme in orange. Starting with identical initial configurations (a) for Stokes and (h) for decoupled viscosity, the highly viscous armadillo and bunny collide and begin rotating through frames 60, 168, 276, 384, 492, and 600 from left to right in figures (b)-(g) for Stokes and (i)-(n) for the decoupled scheme. Our method (blue) better conserves angular momentum of the bunny-armadillo system, leading to faster rotation.

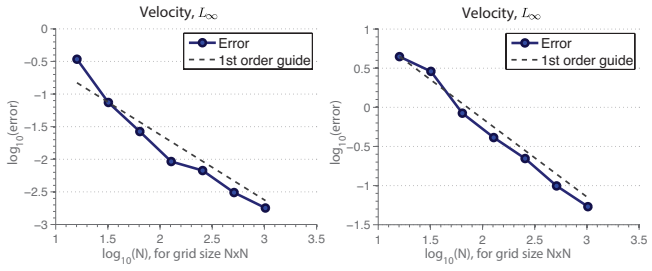

(a) Free surface test (b) Solid wall test

Fig. 10. Log-log error plots showing first order convergence for a single step time for a pair of 2D unsteady Stokes problems.

Example Name	Method	Time	Seconds / Frame	Stokes / Decoupled
Coiling at 25 viscosity	Stokes	01:30:43	9	4.03
	Decoupled	00:22:30	2	
Coiling at 100 viscosity	Stokes	03:50:11	23	1.63
	Decoupled	02:21:15	14	
Piling Armadillos	Stokes	08:52:38	44	4.06
	Decoupled	02:11:05	11	
Colliding Characters	Stokes	00:25:56	3	3.16
	Decoupled	00:08:13	1	
Method Comparisons	Stokes	02:47:18	17	4.82
	Decoupled	00:34:43	3	

Table 1. Timing results (hh:mm:ss), over the length of entire corresponding simulations, comparing the total time of all Stokes solve steps with the total time for all pressure projection and viscosity solve steps in the decoupled case. This compares **only the costs for pressure and viscosity computations**, excluding all other fluid simulator components (advection, extrapolation, etc.). Each animation is 600 frames, except for Piling Armadillos, which is 720 frames long.

6.3 Computational Cost

To solve the Stokes systems, we used the parallelized Jacobi-preconditioned conjugate gradient solver used by Houdini for (decoupled) viscosity. Houdini's pressure solver is more highly optimized (e.g., exploiting the 7-point stencil, etc.), giving it a further advantage over our Stokes prototype. Exploring tailored numerical acceleration strategies (multigrid, preconditioning, etc.) would be a useful future direction. Our examples ranged from 4 to 58 seconds/frame on a machine with a 6 core CPU at 3.4GHz, 32GB of RAM and an NVIDIA Quadro K5000 (4GB) graphics card. We list detailed timing statistics, physical parameters, and machine data for each of our simulations in a supplemental document. Generally, we found that a full Stokes-based simulation approximately ranged between 1.6× and 3.4× the cost for Houdini's decoupled approach, depending on the scenario. This is not surprising, given the larger linear system size. We discuss this cost vs. quality tradeoff below.

In Tables 1 and 2 we show a brief performance comparison between our Stokes-based fluid simulator and the decoupled fluid solver implemented in Houdini. The purpose of these comparisons is to illustrate precisely the overhead cost of employing the Stokes-based simulator in a production setting. The compared simulations contain the same number of timesteps per frame.

7 DISCUSSION AND CONCLUSIONS

We have presented a variational Stokes solver enabling grid-based fluid simulators to reproduce compelling viscous liquid motions with higher visual and physical fidelity than demonstrated previously, while retaining support for features such as moving boundaries, surface tension, and spatially varying viscosity.

Our method's advantages come at the cost of a larger linear system solve at each step compared to decoupled variational viscosity, which is in turn more expensive than per-component Laplacian viscosity. We therefore make the following practical recommendations. For scenarios where viscosity does not vary spatially, and either there is no free surface (e.g., smoke simulation) or realistic rotation/shearing is deemed irrelevant, the Laplacian form is ideal [Carlson et al. 2002]. If buckling or spatially varying viscosity are required and excess smoothing is tolerable, decoupled variational viscosity should be used [Batty and Bridson 2008]. Finally, if one further desires realistic coiling effects, sharper surface details, or greater physical fidelity, our Stokes-based method should be preferred.

Example Name	Method	Time	Seconds / Frame	Stokes / Decoupled
Coiling at 25 viscosity	Stokes	01:48:37	11	3.03
	Decoupled	00:35:50	4	
Coiling at 100 viscosity	Stokes	04:13:56	25	1.56
	Decoupled	02:42:54	16	
Piling Armadillos	Stokes	11:38:50	58	2.49
	Decoupled	04:40:13	23	
Colliding Characters	Stokes	00:39:58	4	1.80
	Decoupled	00:22:09	2	
Method Comparisons	Stokes	03:39:28	22	3.41
	Decoupled	01:04:20	6	
Method Comparisons (timesteps 4.5× smaller)	Decoupled	03:53:43	23	

Table 2. Timing results (hh:mm:ss), over the length of entire corresponding simulations, comparing the Stokes-based fluid solver with decoupled fluid solver in terms of **total cost including all other simulation steps** (advection, extrapolation, etc.). This gives an indication of the overall net impact of the use of the more costly Stokes solver step in Table 1. In the additional supplemental video we compare the Stokes-based simulation with Houdini's simulated with timesteps 4.5× smaller than those used in the Stokes-based simulation. This illustrates that the Stokes simulation can produce higher fidelity surface detail even with a much larger timestep. Each animation is 600 frames, except for Piling Armadillos, which is 720 frames long.

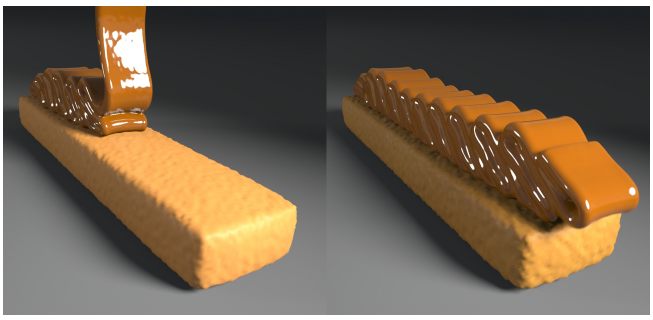

Fig. 11. Smooth buckling of a layer of caramel onto a wafer.

Although we believe our conveyor belt results are attractive, the resulting "sewing patterns" do not have the fidelity of Bergou's specialized thread model [Bergou et al. 2010]; we found the behavior to be quite sensitive to boundary conditions, grid resolution, and other parameters, and look forward to further investigating this scenario. Our supplemental video also shows that with high viscosity and surface tension coefficients in a zero-gravity scenario, the liquid accumulates some translational and rotational drift, although this effect reduces under refinement. We conjecture this is because approximate curvature-based surface tension models (in the vein of ghost fluid) are not strictly conservative, so the integrated net force is often not numerically zero.

Our approach is extensible to two-way solid-fluid coupling by adding appropriate solid energy terms, along the lines of prior work [Batty et al. 2007; Narain et al. 2010]. Similarly, the extension to multiphase flows should be straightforward. It would also be interesting to incorporate our approach into non-Newtonian fluid simulators.

ACKNOWLEDGMENTS

This work was supported in part by the Natural Sciences and Engineering Research Council of Canada (RGPIN-04360-2014, CRDPJ-499952-2016) and Side Effects Software. Thanks to Ryan Goldade for helpful feedback and discussions as well as computing environment support, and to John Lynch for guidance on Houdini FLIP simulations and scenario setup.

REFERENCES

Luiz Fernando de Souza Andrade, Marcos Sandim, Fabiano Petronetto, Paulo Pagliosa, and Afonso Paiva. 2015. Particle-based fluids for viscous jet buckling. *Computers and Graphics* 52 (2015), 106–115.

Basile Audoly, Nicolas Clauvelin, Pierre-Thomas Brun, Miklos Bergou, Eitan Grinspun, and Max Wardetzky. 2012. A discrete geometric approach for simulating the dynamics of thin viscous threads. (2012).

David Baraff. 1996. Linear-time dynamics using Lagrange multipliers. In *SIGGRAPH*. 137–146.

G. K. Batchelor. 1967. *An Introduction to Fluid Dynamics*. Cambridge University Press.

Christopher Batty, Florence Bertails, and Robert Bridson. 2007. A fast variational framework for accurate solid-fluid coupling. *ACM Trans. Graph. (SIGGRAPH)* 26, 3 (2007), 100. http://portal.acm.org/citation.cfm?id=1276502

Christopher Batty and Robert Bridson. 2008. Accurate viscous free surfaces for buckling, coiling, and rotating liquids. In *Symposium on Computer Animation*. 219–228. http://portal.acm.org/citation.cfm?id=1632624

Christopher Batty and Ben Houston. 2011. A simple finite volume method for adaptive viscous liquids. In *Symposium on Computer Animation*. 111–118.

Christopher Batty, Andres Uribe, Basile Audoly, and Eitan Grinspun. 2012. Discrete viscous sheets. *ACM Trans. Graph. (SIGGRAPH)* 31, 4 (2012), 113.

Jan Bender and Dan Koschier. 2016. Divergence-Free SPH for Incompressible and Viscous Fluids. *IEEE TVCG* 99 (2016).

Michele Benzi, Gene H. Golub, and Jorg Liesen. 2005. Numerical solution of saddle point problems. *Acta Numerica* 14 (2005), 1–37.

Miklos Bergou, Basile Audoly, Etienne Vouga, Max Wardetzky, and Eitan Grinspun. 2010. Discrete viscous threads. *ACM Trans. Graph. (SIGGRAPH)* 29, 4 (2010), 116.

Andrea Bonito, Marco Picasso, and Manuel Laso. 2006. Numerical simulation of 3D viscoelastic flows with free surfaces. *J. Comp. Phys.* 215, 2 (2006), 691–716.

Robert Bridson. 2015. *Fluid simulation for computer graphics, 2nd edition*. A. K. Peters, Ltd.

Pierre-Thomas Brun, Neil Ribe, and Basile Audoly. 2012. A numerical investigation of the fluid-mechanical sewing machine. *Phys. Fluids* 24, 4 (2012), 043102.

Mark Carlson, Peter J. Mucha, R. Van Horn, and Greg Turk. 2002. Melting and flowing. In *Symposium on Computer Animation*. 167–174.

Pascal Clausen, Martin Wicke, Jonathan Richard Shewchuk, and James F. O'Brien. 2013. Simulating liquids and solid-liquid interactions with Lagrangian meshes. *ACM Trans. Graph.* 32, 2 (2013), 17.

M. S. Darwish, J. R. Whiteman, and M. J. Bevis. 1992. Numerical modelling of viscoelastic liquids using a finite-volume method. *Journal of Non-Newtonian Fluid Mechanics* 45, 3 (1992), 311–337.

Gilles Daviet and Florence Bertails-Descoubes. 2016. A semi-implicit material point method for the continuum simulation of granular materials. *ACM Trans. Graph. (SIGGRAPH)* (2016).

Mathieu Desbrun and Marie-Paule Gascuel. 1996. Smoothed particles: a new paradigm for animating highly deformable bodies. In *Eurographics Workshop on Computer Animation and Simulation*. 61–76.

Howard Elman. 2002. Preconditioners for saddle point problems arising in computational fluid dynamics. *Applied Numerical Mathematics* 43, 1-2 (2002), 75–89.

Doug Enright, Duc Nguyen, Frédéric Gibou, and Ron Fedkiw. 2003. Using the particle level set method and a second order accurate pressure boundary condition for free surface flows. In *Proceedings of the 4th ASME-JSME Joint Fluids Engineering Conference*. ASME, 337–342.

Kenny Erleben, Marek Misztal, and Andreas Baerentzen. 2011. Mathematical foundation of the optimization-based fluid animation method. In *Symposium on Computer Animation*. 101–110.

Henrik Fält and Doug Roble. 2003. Fluids with extreme viscosity. In *SIGGRAPH Sketches*. 1.

Nick Foster and Dimitris Metaxas. 1996. Realistic animation of liquids. *Graphical Models and Image Processing* 58, 5 (1996), 471–483. http://portal.acm.org/citation.cfm?id=244315

Theodore F. Gast, Craig Schroeder, Alexey Stomakhin, Chenfanfu Jiang, and Joseph M. Teran. 2015. Optimization integrator for large time steps. *IEEE TVCG* 21, 10 (2015), 1103–1115.

Tolga G. Goktekin, Adam W. Bargteil, and James F. O'Brien. 2004. A method for animating viscoelastic fluids. *ACM Trans. Graph. (SIGGRAPH)* 23, 3 (aug 2004),

463–468. DOI: https://doi.org/10.1145/1015706.1015746
Rony Goldenthal, David Harmon, Raanan Fattal, Michel Bercovier, and Eitan Grinspun. 2007. Efficient simulation of inextensible cloth. *ACM Trans. Graph. (SIGGRAPH)* 26, 3 (2007), 49.
Jeong-Mo Hong and Chang-Hun Kim. 2005. Discontinuous fluids. *ACM Trans. Graph. (SIGGRAPH)* 24, 3 (jul 2005), 915–920. DOI: https://doi.org/10.1145/1073204.1073283
Chenfanfu Jiang, Craig Schroeder, Andrew Selle, Joseph Teran, and Alexey Stomakhin. 2015. The affine particle-in-cell method. *ACM Trans. Graph. (SIGGRAPH)* 34, 4 (2015), 51.
Nahyup Kang, Jinho Park, Junyong Noh, and Sung Yong Shin. 2010. A hybrid approach to multiple fluid simulation using volume fractions. *Computer Graphics Forum (Eurographics)* 29, 2 (2010), 685–694.
Gergely Klar, Theodore Gast, Andre Pradhana, Chuyuan Fu, Craig Schroeder, Chenfanfu Jiang, and Joseph Teran. 2016. Drucker-Prager elastoplasticity for sand animation. *ACM Trans. Graph. (SIGGRAPH)* (2016).
Benjamin Lalanne, Lucia Rueda Villegas, Sebastian Tanguy, and Frederic Risso. 2015. On the computation of viscous terms for incompressible two-phase flows with Level Set/Ghost Fluid Method. *J. Comput. Phys.* 301 (2015), 289–307.
David I. W. Levin, Joshua Litven, Garret L. Jones, Shinjiro Sueda, and Dinesh K. Pai. 2011. Eulerian solid simulation with contact. *ACM Trans. Graph. (SIGGRAPH)* (2011).
Frank Losasso, Tamar Shinar, Andrew Selle, and Ronald Fedkiw. 2006. Multiple interacting liquids. *ACM Trans. Graph. (SIGGRAPH)* 25, 3 (2006), 812–819.
Sebastian Martin, Bernhard Thomaszewski, Eitan Grinspun, and Markus Gross. 2011. Example-based elastic materials. *ACM Trans. Graph. (SIGGRAPH)* 30, 4 (2011), 72.
Chohong Min and Frédéric Gibou. 2007. Geometric integration over irregular domains with application to level-set methods. *J. Comp. Phys.* 226, 2 (oct 2007), 1432–1443. DOI: https://doi.org/10.1016/j.jcp.2007.05.032
Marek Misztal, Robert Bridson, Kenny Erleben, Andreas Baerentzen, and Francois Anton. 2010. Optimization-based fluid simulation on unstructured meshes. In *VRIPHYS*.
Marek Misztal, Kenny Erleben, Adam W. Bargteil, B. Bunch Christensen, Andreas Baerentzen, and Robert Bridson. 2012. Multiphase flow of immiscible fluids on unstructured moving meshes. In *Symposium on Computer Animation*. Eurographics Association, Lausanne, Switzerland, 97–106.
G. Mompean and M. Deville. 1997. Unsteady finite volume simulation of Oldroyd-B fluid through a three-dimensional planar contraction. *Journal of Non-Newtonian Fluid Mechanics* 72, 2-3 (oct 1997), 253–279. DOI: https://doi.org/10.1016/S0377-0257(97)00033-5
Patrick Mullen, Keenan Crane, Dmitry Pavlov, Yiying Tong, and Mathieu Desbrun. 2009. Energy-preserving integrators for fluid animation. *ACM Trans. Graph. (SIGGRAPH)* 28, 3 (2009), 38. http://portal.acm.org/citation.cfm?id=1531326.1531344
Rahul Narain, Abhinav Golas, and Ming C. Lin. 2010. Free-flowing granular materials with two-way solid coupling. *ACM Trans. Graph. (SIGGRAPH Asia)* 29, 6 (2010), 173.
Rahul Narain, Jason Sewall, Mark Carlson, and Ming C. Lin. 2008. Fast animation of turbulence using energy transport and procedural synthesis. *ACM Trans. Graph. (SIGGRAPH Asia)* 27, 5 (2008), 166. http://portal.acm.org/citation.cfm?id=1457515.1409119
Yen Ting Ng, Chohong Min, and Frédéric Gibou. 2009. An efficient fluid-solid coupling algorithm for single-phase flows. *J. Comp. Phys.* 228, 23 (2009), 8807–8829.
Michael B. Nielsen and Brian B. Christensen. 2010. Improved variational guiding of smoke animations. *Computer Graphics Forum (Eurographics)* 29, 2 (2010), 705–712.
Cassio M. Oishi, Murilo F. Tomé, José A. Cuminato, and Sean McKee. 2008. An implicit technique for solving 3D low Reynolds number moving free surface flows. *J. Comp. Phys.* 227, 16 (2008), 7446–7468.
Andreas Peer, Markus Ihmsen, Jens Cornelis, and Matthias Teschner. 2015. An implicit viscosity formulation for SPH fluids. *ACM Trans. Graph. (SIGGRAPH)* 34, 4 (2015), 114.
Andreas Peer and Matthias Teschner. 2016. Prescribed velocity gradients for highly viscous SPH fluids with vorticity diffusion. *IEEE TVCG* (2016).
Daniel Ram, Theodore Gast, Chenfanfu Jiang, Craig Schroeder, Alexey Stomakhin, Joseph Teran, and Pirouz Kavehpour. 2015. A material point method for viscoelastic fluids, foams and sponges. In *Symposium on Computer Animation*. 157–163.
Nick Rasmussen, Doug Enright, Duc Nguyen, Sebastian Marino, N. Sumner, Willi Geiger, Samir Hoon, and Ron Fedkiw. 2004. Directable photorealistic liquids. In *Symposium on Computer Animation*. 193–202.
Neil Ribe, Mehdi Habibi, and Daniel Bonn. 2012. Liquid rope coiling. *Annual review of fluid mechanics* 44 (2012), 249–266.
Avi Robinson-Mosher, R. Elliot English, and Ronald Fedkiw. 2009. Accurate tangential velocities for solid fluid coupling. In *Symposium on Computer Animation*. 227–236. http://portal.acm.org/citation.cfm?id=1599470.1599500
Avi Robinson-Mosher, Craig Schroeder, and Ron Fedkiw. 2011. A symmetric positive definite formulation for monolithic fluid structure interaction. *J. Comp. Phys.* 230, 4 (2011), 1547–1566. http://physbam.stanford.edu/
Avi Robinson-Mosher, Tamar Shinar, Jon Gretarsson, Jonathan Su, and Ronald Fedkiw. 2008. Two-way coupling of fluids to rigid and deformable solids and shells. *ACM Trans. Graph. (SIGGRAPH)* 27, 3 (2008), 46. http://portal.acm.org/citation.cfm?id=1399504.1360645
Allen Ruilova. 2007. Creating realistic CG honey. In *SIGGRAPH Posters*. 58.
Craig Schroeder, Alexey Stomakhin, Russel Howes, and Joseph M. Teran. 2014. A second order virtual node algorithm for NavierâĂŞStokes flow problems with interfacial forces and discontinuous material properties. *J. Comp. Phys.* 265 (2014), 221–245.
Rajsekhar Setaluri, Mridul Aanjaneya, Sean Bauer, and Eftychios Sifakis. 2014. SPGrid: A sparse paged grid structure applied to adaptive smoke simulation. *ACM Trans. Graph. (SIGGRAPH Asia)* 33, 6 (2014), 205.
Side Effects Software. 2016. Houdini. (2016).
Alexey Stomakhin, Craig Schroeder, Lawrence Chai, Joseph Teran, and Andrew Selle. 2013. A material point method for snow simulation. *ACM Trans. Graph. (SIGGRAPH)* 32, 4 (2013), 102.
Alexey Stomakhin, Craig Schroeder, Chenfanfu Jiang, Lawrence Chai, Joseph Teran, and Andrew Selle. 2014. Augmented MPM for phase-change and varied materials. *ACM Trans. Graph. (SIGGRAPH)* 33, 4 (2014), 138.
M. Sussman, K.M. Smith, M.Y. Hussaini, M. Ohta, and R. Zhi-Wei. 2007. A sharp interface method for incompressible two-phase flows. *J. Comp. Phys.* 221 (2007), 469–505.
Tetsuya Takahashi, Yoshinori Dobashi, Issei Fujishiro, Tomoyuki Nishita, and Ming C. Lin. 2015. Implicit formulation for SPH-based viscous fluids. *Computer Graphics Forum (Eurographics)* 34, 2 (2015), 493–502.
Murilo F. Tomé, L. Grossi, Antonio Castelo, José A. Cuminato, Norberto Mangiavacchi, Valdemir G. Ferreira, F. S. de Sousa, and Sean McKee. 2004. A numerical method for solving three-dimensional generalized Newtonian free surface flows. *Journal of Non-Newtonian Fluid Mechanics* 123, 2-3 (2004), 85–103.
Murilo F. Tomé and Sean McKee. 1994. GENSMAC: A computational marker and cell method for free surface flows in general domains. *J. Comp. Phys.* 110, 1 (1994), 171–186.
M F Tomé and Sean McKee. 1999. Numerical simulation of viscous flow: Buckling of planar jets. *International Journal for Numerical Methods in Fluids* 29, 6 (1999), 705–718.
Maxime Tournier, Matthieu Nesme, Benjamin Gilles, and Francois Faure. 2015. Stable constrained dynamics. *ACM Trans. Graph. (SIGGRAPH)* 34, 4 (2015), 132.
Mark Wiebe and Ben Houston. 2004. The Tar Monster: Creating a character with fluid simulation. In *SIGGRAPH Sketches*.
Yonghao Yue, Breannan Smith, Christopher Batty, Changxi Zheng, and Eitan Grinspun. 2015. Continuum foam: A material point method for shear-dependent flows. *ACM Trans. Graph. (SIGGRAPH)* 34, 5 (2015), 160.
Xinxin Zhang and Robert Bridson. 2015. Restoring the missing vortices in advection-projection fluid solvers. *ACM Trans. Graph. (SIGGRAPH)* 34, 4 (2015), 52.
Bo Zhu, Minjae Lee, Ed Quigley, and Ronald Fedkiw. 2015. Codimensional non-Newtonian fluids. *ACM Trans. Graph. (SIGGRAPH)* 34, 4 (2015), 115.
Bo Zhu, Ed Quigley, Matthew Cong, Justin Solomon, and Ronald Fedkiw. 2014. Codimensional surface tension flow on simplicial complexes. *ACM Trans. Graph. (SIGGRAPH)* 33, 4 (2014), 111.